Scatterer size estimation in pulse-echo ultrasound using focused sources: Calibration measurements and phantom experiments

Timothy A. Bigelow and William D. O'Brien, Jr.[a)]
Bioacoustics Research Laboratory, Department of Electrical and Computer Engineering, University of Illinois, 405 North Mathews, Urbana, Illinois 61801

(Received 13 June 2003; revised 31 March 2004; accepted 12 April 2004)

In a companion paper [T. A. Bigelow and W. D. O'Brien Jr., J. Acoust. Soc. Am. **116**, 578 (2004)], theory, supported by simulations, showed that accurate scatterer size estimates could be obtained using highly focused sources provided that the derived generalized attenuation-compensation function was used and the velocity potential field near the focus could be approximated as a three-dimensional Gaussian. Herein, the theory is further evaluated via experimental studies. A calibration technique is developed to find the necessary equivalent Gaussian dimensions for a focused source using reflections obtained from a rigid plane scanned through the focus. Then, the theoretical analysis of focused sources is validated experimentally using three spherically focused ultrasound transducers to estimate the radius of glass beads imbedded in tissue mimicking phantoms. Both the impact of focusing ($f/1$, $f/2$, and $f/4$) and the effect of scatterer type (comparing glass bead results to simulation results that used scatterers with Gaussian impedance distributions) were tested. The simulated differences agree with the measured differences to within 2.5% provided that the comparison is made between the same scatterer type and sources with the same equivalent Gaussian dimensions. The improvement provided by the generalized attenuation-compensation function is greatly influenced by the type of scatterer whose size is being estimated and decreases as the wavelength dependence of the Gaussian depth of focus is reduced. [DOI: 10.1121/1.1757453]

PACS numbers: 43.80.Qf, 43.80.Vj [FD] Pages: 594–602

Pages: 594–602 Pages: 594–602602

LIST OF SYMBOLS

$A_{current}$	attenuation-compensation function currently being used by the estimator (i.e., A_{comp}, A_{OO}, A_{OM}, or A_{PC}).
A_{comp}	complete attenuation-compensation function including focusing effects along the beam axis [i.e., $A_{comp}(\omega)=e^{4\alpha_{eff}z_T}/(\int_{-L/2}^{L/2}ds_z g_{win}(s_z)e^{-4(s_z^2/w_z^2)}e^{4\alpha s_z})$].
a_{eff}	estimated radius of glass beads.
A_{OO}	Oelze–O'Brien attenuation-compensation function [i.e., $A_{OO}(\omega)=(e^{4\alpha_{eff}z_T}e^{-4\alpha L/2}/L)(2\alpha L/(1-e^{-2\alpha L}))^2$].
A_{OM}	O'Donnell–Miller attenuation-compensation function [i.e., $A_{OM}(\omega)=4\alpha e^{4\alpha_{eff}z_T}/(e^{4\alpha L/2}-e^{-4\alpha L/2})$].
A_{PC}	point attenuation-compensation function [i.e., $A_{PC}(\omega)=e^{4\alpha_{eff}z_T}/L$].
ASD	average squared difference term minimized when estimating scatterer size.
c	small-signal sound speed of phantom.
c_o	small-signal sound speed of water.
F	form factor describing power spectral density function for scatterer.
$f\#$	f-number for a spherically focused source.
f_R	principle frequency of Rayleigh distribution [i.e., $f\cdot\exp(-((f-f_R)/\sigma_R)^2)$].
G_o	geometric gain value for pressure field at focus when W_{source} is approximated by a Gaussian (units of m).
H	dimensionless filtering characteristics for the ultrasound source.
k_o	wave number in water.
L	total width of rectangular windowing function.
PII	pulse intensity integral.
S_T	aperture area of ultrasound transmitter.
T_{win}	total width of rectangular windowing function applied to time-domain waveform (i.e., $T_{win}=2L/c$).
V'	volume containing glass beads contributing to the scattered signal.
V_{inc}	voltage applied to the ultrasound source during transmit.
V_{plane}	voltage from ultrasound source due to the backscatter from rigid plane near focus.
V_{refl}	voltage from ultrasound source due to the backscatter from glass beads.
w_x, w_y, w_z	equivalent Gaussian dimensions of velocity potential field in focal region.
w_{zb}	intercept term for equivalent Gaussian depth of focus as a function of wavelength (i.e., $w_z=w_{zm}\cdot\lambda+w_{zb}$).
w_{zm}	slope term for equivalent Gaussian depth of focus as a function of wavelength (i.e., $w_z=w_{zm}\cdot\lambda+w_{zb}$).

[a)]Author to whom all correspondence should be addressed. Electronic mail: wdo@uiuc.edu

X log difference between calibrated scattered spectrum and form factor used in minimization.

$\overline{X}$ mean value of X over bandwidth of minimization.

z_f distance of rigid plane used to acquire reference waveform to the focal plane.

z_T distance of aperture plane of the ultrasound transmitter/detector to the focal plane.

α attenuation in the scattering region, V'.

α_{eff} effective attenuation for all tissue between focal plane and aperture plane (i.e., total attenuation along beam axis$=\alpha_{eff} z_T$).

α_o slope of attenuation in the scattering region assuming strict linear frequency dependent attenuation (i.e., $\alpha=\alpha_o \cdot f$).

λ wavelength.

λ_0 the wavelength corresponding to the spectral peak from the reference spectrum (i.e., V_{plane}) used when calculating the depth of field (i.e., $7.08\lambda_0 f\#^2$) to normalize the window length.

σ_R bandwidth of Rayleigh distribution [i.e., $f \cdot \exp(-((f-f_R)/\sigma_R)^2)$].

I. INTRODUCTION

Quantifying the ultrasonic backscatter returned from a medium of interest has been important in many different applications of acoustics ranging from nondestructive testing[1] to tissue imaging.[2] Regardless of the application, the goal remains the same: use the statistics of the frequency envelope of the backscattered signal to estimate the size of the scatterer in the medium. This involves first developing an impedance distribution to describe the scattering (model), and then fitting the measured backscattered data to the model to determine the mean scatterer size.[2–5]

Most of the models developed previously have assumed that large *f*-numbers are required to accurately extract information on the microstructure of the medium.[3,5,6] However, in our companion paper,[7] we have shown that smaller *f*-numbers can be used provided that the velocity potential field is modeled as a three-dimensional Gaussian beam in the focal region, and the correct generalized attenuation-compensation function is used. The companion paper restricted its attention to computer simulations of ideal sources where the impedance of the scatterers varied according to a Gaussian distribution. Hence, the impact of different scatterer types and nonideal beams was not addressed. A Gaussian impedance distribution is commonly assumed when analyzing the backscatter from biological tissues,[8] but the exact impedance distribution for tissue scatterers remains to be determined. Therefore, any relationship between the type of scatterer and the accuracy of the estimates of scatterer size for focused sources should be investigated.

In this paper, we build upon our previous work[7] by using real rather than ideal sources and by considering glass bead scatterers instead of scatterers with a Gaussian impedance distribution (Gaussian scatterer). The power spectral density functions (or form factors) for these two types of scatterers are very different,[5] and are given by

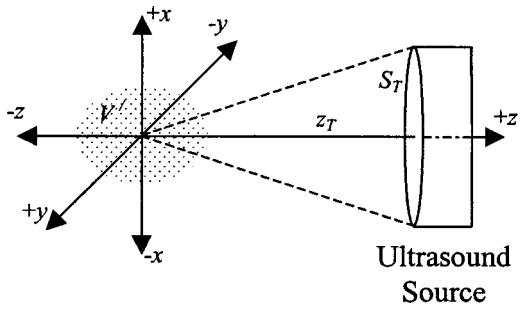

FIG. 1. Coordinate system selected for experiment.

$$F(k)=\begin{cases}\left[\dfrac{\sin(2ka_{eff})}{2ka_{eff}}\right]^2 & (Bead),\\ e^{-0.827k^2a_{eff}^2} & (Gaussian).\end{cases} \quad (1)$$

The form factor approximating the glass bead falls off much faster with increasing scatterer radius than does the Gaussian scatterer.[5]

Because the sources are real, the first challenge is to measure the equivalent frequency-dependent Gaussian beamwidths, w_x and w_y, and Gaussian depth of focus, w_z, of the field in the focal region. Two different methods are examined using a spherically focused transducer, and the results from the two methods are compared. One of the methods is then used to find the equivalent Gaussian depth of focus for three spherically focused transducers ($f/1$, $f/2$, and $f/4$). These three transducers are then used experimentally to obtain scatterer size estimates for an ultrasound phantom containing glass beads. Then, the effect of scatterer type is assessed by repeating the simulations using glass bead scatterers and comparing the bead simulation and phantom results to our earlier simulation results[7] that used scatterers with Gaussian impedance distributions. Likewise, the influence of the wavelength dependence of w_z of the sources is investigated through more computer simulations and analytical calculations. In the last section of the paper, some conclusions based on the experimental results are provided with the hope of guiding future investigators.

II. GAUSSIAN DIMENSION MEASUREMENTS

There are many possible methods for determining the equivalent Gaussian dimensions (beamwidth and depth of focus) of an ultrasound source, two of which were compared experimentally in our investigation. The evaluation was done using a spherically focused $f/2$ transducer (Valpey Fisher Instruments, Inc., Hopkinton, MA) with a diameter of 2.1 cm, a center frequency of 8.7 MHz, and a -3 dB bandwidth of 1.6 MHz as measured from a wire reflection.[9] The transducer was placed in a water bath and shock excited using a Panametrics 5900 pulser/receiver (Waltham, MA) operating in pulse-echo mode, and the returned waveforms were recorded using a digital oscilloscope at a sampling frequency of 100 MHz (Lecroy 9354 TM, Chestnut Ridge, NY). The coordinate system for the experiment is shown in Fig. 1. Although a spherically focused transducer was selected for the evaluation, the experimental techniques can be applied to any focused source including dynamically focused arrays.

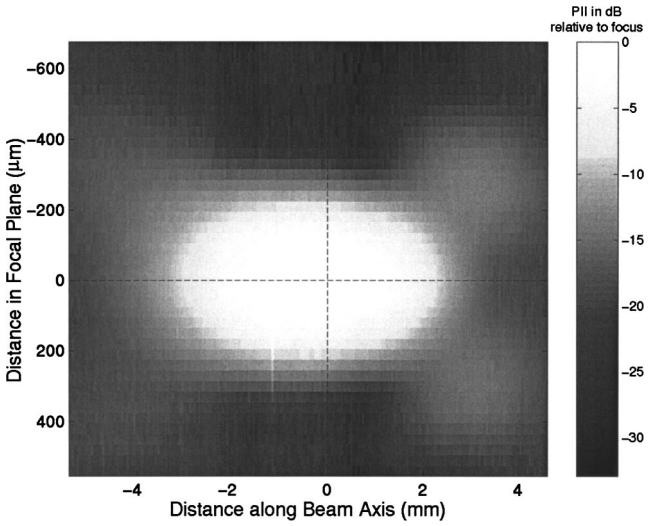

FIG. 2. Image of *PII* in dB showing location of field axes (dotted line) for the Gaussian dimension measurement from the wire reflections.

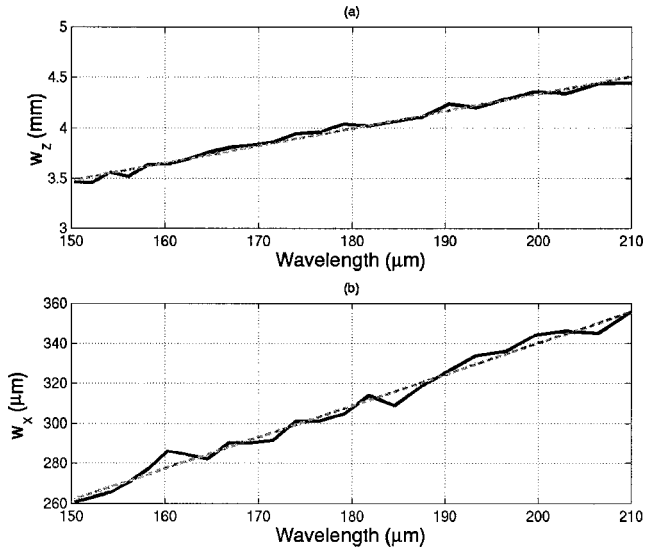

FIG. 3. Measured Gaussian dimensions and the resulting linear fits for the beam axis (a) and the focal plane axis (b) from the wire reflections.

A. Gaussian dimensions from wire

The first method considered for determining the Gaussian dimensions was the traditional technique of passing a wire target systematically through the entire ultrasound beam in a water bath and recording the pulse/echo waveform for each field location.[9] The wire target is then assumed to approximate a point target (i.e., neglect integration of wire across beam). In order to insure that the correct dimensions were measured, the wire needs to be moved throughout the entire field because it is difficult to align the beam axis with the scan axis when using a wire. In our experiment, the 38-μm-diam tungsten wire (California Fine Wire Company, Grover City, CA) was moved in a rectangular grid of dimension 10 mm by 1.2 mm in steps of 50 and 30 μm, respectively, using a Daedal microprecision positioning system (Daedal Inc., Harrison City, PA). The pulse intensity integral (PII) was then calculated for the return echo from every wire location yielding a map of the beam pattern. From the PII beam pattern, the beam axis (z axis) and focal plane axis (x axis) were determined. An image showing the log-compressed PII beam pattern along with the field axes is shown in Fig. 2. For arrays or other beams lacking circular symmetry in the focal plane, the experiment would need to be repeated with the wire target rotated so that the field intensity at each frequency along the y axis could also be obtained.

Once the field axes were determined, the magnitude of the Fourier transform for each waveform at each location along the axes was calculated yielding the field intensity at each frequency and axial position. The field intensities for frequencies between 7 and 10 MHz versus the location on the field axes were then normalized and fit by a Gaussian distribution yielding the appropriate frequency-dependent Gaussian dimensions. Also, the location of the focus was allowed to change for the different frequencies because this has been shown to improve the accuracy of the Gaussian approximation.[7] Working with the normalized field intensity at each frequency was equivalent to working with the square of the velocity potential when finding the Gaussian dimensions. Finally, a linear fit was performed on the measured dimensions versus the acoustic wavelength yielding frequency-dependent Gaussian dimensions of $w_z = 17.1\lambda + 924 \cdot 10^{-6}$ m and $w_x = 1.57\lambda + 27.0 \cdot 10^{-6}$ m. Plots showing the measured dimensions and the resulting linear fits are shown in Fig. 3. When λ goes to zero, the beamwidths and depth of focus do not go to zero due to the intercept term. This intercept term is ~25 times larger than the intercept term found for the ideal focused source.[7] Hence, the large intercept results from the sources not being ideally diffraction limited.

The determination of the frequency-dependent Gaussian dimensions of a source using the wire technique is robust. However, it is very time consuming due to the need to map out most of the acoustic field, a problem that is only compounded by diagnostically relevant fields. Furthermore, it provides more information than is required (i.e., w_x). In the companion paper,[7] we demonstrated that in order to correct for focusing along the beam axis when determining the scatterer size we only need to know w_z. Hence, in the next section we explore a faster measurement technique that only yields w_z and is also a simple extension to the calibration methods currently used to obtain a reference in scatterer size estimates.[2,3,5,10]

B. Gaussian dimensions from rigid plane

The second method used to obtain the equivalent frequency-dependent Gaussian dimensions is based on the theoretical backscattered signal from a rigid plane positioned near the focal plane given by[7]

$$V_{plane}(\omega) = \frac{-2\pi w_x w_y k_o^2 G_o^2 V_{inc}(\omega) H^2(\omega)}{S_T (4\pi)^2} \times e^{i2k_o(z_T - z_f)} e^{-2(z_f/w_z)^2}. \quad (2)$$

A measurement for w_z can be obtained from Eq. (2) by varying the location of the plane in the focal region, z_f. Equation (2) includes a complete description of the reflection from the

TABLE I. Relevant properties of transducers used in the phantom experiments.

f#	Center frequency (MHz)	−3 dB bandwidth (MHz)	Transducer diameter (cm)	Scan length (step size) to find w_z	w_z	Depth into phantom (mm)
1	8.7	1.5	2.1	−2 mm→2 mm (50 μm)	$3.22\lambda + 1285$ μm	6
2	8.7	1.6	2.1	−2 mm→2 mm (150 μm)	$16.1\lambda + 802$ μm	12.5
4	9.4	3.8	1.4	−8 mm→8 mm (200 μm)	$76.8\lambda + 4207$ μm	15

plate, unlike the wire technique that neglected the field integration along its length, provided that the velocity potential field from the source obeys a Gaussian distribution. Therefore, the measurement should only be made in the focal region where the Gaussian approximation is valid and secondary field properties (i.e., side lobes and waveform curvature) can be neglected.

Hence, a smooth Plexiglas surface was initially positioned 2 mm past the focal plane for the transducer in a water bath ($z_f = -2$ mm). The Plexiglas was then moved along the beam axis passing through the focus in steps of 150 μm until it was 2 mm in front of the focus ($z_f = 2$ mm) using the Daedal microprecision positioning system, and the echo waveforms were recorded for each Plexiglas location. The magnitude of the Fourier transform was then calculated for each of the acquired waveforms. The resulting magnitude spectra were then divided by the spectrum obtained for the Plexiglas located at the focal plane ($z_f = 0$) for frequencies between 7 and 10 MHz (i.e., normalized for each frequency) and fit by a Gaussian distribution yielding the equivalent Gaussian depth of focus, w_z. Then, a linear fit was performed on the measured depth of focus versus wavelength yielding a frequency-dependent Gaussian depth of focus of $w_z = 16.1\lambda + 802 \cdot 10^{-6}$ m which differed by less than 7.6% from depth of focus found using the wire technique. Therefore, the two methods for measuring the frequency-dependent Gaussian depth of focus along the beam axis, w_z, are equivalent. Due to the reduced measurement time, the measurement of the depth of focus using the rigid plane was also used to determine the w_z values for the other sources used in the phantom experiments. These values are provided in Table I along with the scan length the planar reflector was moved when acquiring the reflections. Variations in the scan length about 4 mm did not significantly change the resulting w_z values, indicating secondary field properties did not dramatically affect the measured Gaussian depth of focus for this scan length.

III. PHANTOM EXPERIMENTS

The phantom experiments were designed to validate the use of focused sources in predicting scatterer size as well as investigate the effects of focusing along the beam axis in greater detail. Hence, the three transducers described in Table I were used to estimate the radius of glass beads in a tissue mimicking phantom. The reported center frequencies and −3 dB bandwidths had been previously measured by a wire reflection technique.[9]

A. Experimental procedure and initial results

The agar phantom used in the experiment was produced at the University of Wisconsin and was part of an interlaboratory comparison of ultrasonic backscatter, attenuation, and sound speed measurements.[11] The phantom consisted of degassed water, agar, *n*-proponal, finely powdered graphite, and glass beads whose radii varied between 22.5 and 26.5 μm with an average concentration of 20.454/mm^3. The attenuation of the phantom (0.55 ± 0.08 dB/cm/MHz) was measured by both insertion loss techniques as well as by observing the change in backscatter with propagation depth into the phantom at room temperature. The sound speed of the phantom was reported by Madsen *et al.*[11] to have a mean value of 1534.4 m/s at 22 °C with a temperature dependence of 1.7 m/s/°C.

The experiments were performed by first positioning a rigid plane at the focus of the transducer in a degassed water bath. The transducers were shock excited using a Panametrics 5900 pulser/receiver operating in pulse-echo mode, and the echo waveforms were captured using a Lecroy 9354 TM digital oscilloscope with a sampling frequency of 100 MHz. The focus was defined as the plane location that resulted in the largest peak–peak voltage for the returned echo waveform. This echo waveform was then recorded as the reference waveform, V_{plane}. The rigid plane used to obtain the reference waveform was made of either Plexiglas or polished metal. The plane was then moved along the beam axis so that the values of w_z could be determined as described previously.

The phantom was then placed such that the reflection from the front surface of the phantom corresponded in time with the previously acquired reference waveform, thereby positioning the front surface of the phantom in the focal plane of the transducer. The focus was then moved into the phantom a known distance by using the Daedal microprecision positioning system. Care was taken so that secondary reflections between the surface of the transducer and the surface of the phantom did not interfere with the speckle from the glass beads. The distance the focus was moved into the phantom for each transducer is also given in Table I. After positioning the focus, 25 independent rf echoes were acquired by moving the phantom along a square grid parallel to the focal plane using the Daedal microprecision positioning system. The grid consisted of five columns and five rows each separated by a distance of 450 μm, 450 μm, and 1 mm for the $f/1$, $f/2$, and $f/4$ transducers, respectively. For each grid position, the echo waveform was averaged between

1000 and 2200 times to remove as much electronic noise as possible.

During processing, each rf echo was windowed by a rectangular gating function centered at the focus, the location of which was known from the reference signal. A rectangular gating function was selected because the traditional attenuation-compensation functions (A_{OO} and A_{OM}) are defined for a rectangular gate. The positioning was done by measuring the water temperature, calculating the sound speed of the water/phantom medium (c_o and c) from the temperature, and then using these sound speeds to position the window at the correct location in time. The length of the gating functions varied from 1 to 13 mm in steps of 0.5 mm with corresponding time gates given by $T_{win}=2L/c$. After windowing, the magnitudes of the Fourier transforms for each rf echo were averaged together yielding an estimate for $E[|V_{refl}(\omega)|^2]$. An estimate for the radius of the glass beads was then obtained by finding the value of a_{eff} that minimized the average squared difference (*ASD*) given,[5]

$$ASD=\underset{\omega}{\text{mean}}[(X(\omega,a_{eff})-\overline{X}(a_{eff}))^2], \tag{3}$$

where

$$\begin{aligned} X(\omega,a_{eff}) &= \ln\left(\frac{E[|V_{refl}(\omega)|^2]}{|V_{plane}(\omega)|^2 k_o^4}\right)+\ln(A_{current}(\omega)) \\ &\quad -\ln\left(\left[\frac{\sin(2ka_{eff})}{2ka_{eff}}\right]^2\right), \\ \overline{X}(a_{eff}) &= \underset{\omega}{\text{mean}}[X(\omega,a_{eff})]. \end{aligned} \tag{4}$$

For the purpose of comparison, the minimization was done for frequencies in the range of 6.5 to 10.5 MHz for all three of the transducers.

The average values of the glass bead radius for window lengths between 3 and 8 mm found using the generalized attenuation-compensation function were 26.1, 22.8, and 22.9 μm for the $f/1$, $f/2$, and $f/4$ transducers, respectively. Hence, the estimated bead radius was well within the range of bead radii known to be in the phantom (i.e., 22.5 to 26.5 μm). In the companion paper,[7] it was shown that the differences between the different attenuation-compensation functions should be relatively constant between different scatterer distributions even though the absolute errors would vary. Hence, the percent difference between the traditional attenuation-compensation functions and the generalized attenuation-compensation function relative to the mean glass bead radius of 24.5 μm was used in the remainder of our evaluation.

The percent difference versus window length for each of the transducers is shown in Fig. 4. λ_0 was the wavelength corresponding to the spectral peak from the reference spectrum (i.e., V_{plane}). The traditional attenuation-compensation functions, A_{PC}, A_{OM}, and A_{OO}, all predict larger bead sizes than the generalized attenuation-compensation function for the $f/1$ and $f/2$ transducers. Also, for the $f/4$ transducer, A_{PC} gives a smaller estimate while A_{OM} and A_{OO} continue to give larger estimates. This same qualitative behavior was

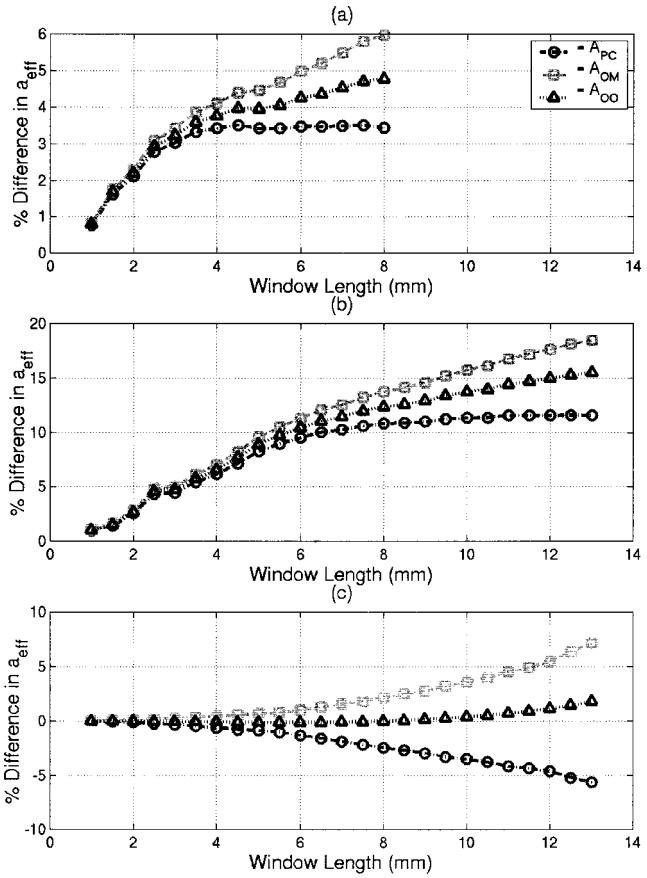

FIG. 4. Experimental results for % differences in a_{eff} versus window length found using traditional attenuation-compensation functions (A_{PC}, A_{OM}, and A_{OO}) as compared to a_{eff} found using A_{comp} for a glass bead phantom with an attenuation of 0.55 ± 0.08 dB/cm/MHz, a concentration of 20.454 beads/mm^3, and a mean bead radius of 24.5 μm from spherically focused transducers with *f*-numbers of (a) $f/1$, (b) $f/2$, and (c) $f/4$.

also observed in our earlier simulation study reported in the companion paper.[7] However, there was not quantitative agreement in the amount of improvement provided by the new generalized attenuation-compensation function.

In the companion paper,[7] the generalized attenuation-compensation function gave an improvement in the scatterer size estimate of 40% to 50% over the traditional attenuation-compensation functions for the $f/2$ transducer with a window length of 13 mm and an attenuation of 0.5 dB/cm/MHz. In the experiment, the $f/2$ transducer only gave an improvement of 12% to 18%. Likewise, the improvement in the experiment for the $f/1$ transducer was only about 3.5% to 6% when our previous simulation study[7] predicted an improvement of 35% to 55%. Also, the $f/1$ transducer yielded improvements in the scatterer size estimate much smaller than the $f/2$ transducer when our previous simulation study[7] indicated that the amount of improvement should plateau at approximately the same values as the window length is increased for both transducers. Even the $f/4$ transducer had less improvement in the experiment (i.e., 7.1% for A_{comp} compared to A_{OM} at 13 mm) as compared to our earlier simulation study[7] (i.e., 17% for A_{comp} compared to A_{OM} at 13 mm). Clearly, these differences in the improvements in the scatterer size estimate when using A_{comp} in the experiment as compared to our earlier simulations[7] need to be understood.

B. Effect of scatterer type

The most obvious difference between our previous simulation study[7] and the phantom experiments is the type of scatterer. Our earlier simulation study[7] used scatterers with Gaussian impedance distributions (i.e., assumed impedance distribution for tissue) whereas the experimental study used glass beads. The form factor for glass beads has a stronger dependence on the scatterer size than does the form factor for Gaussian scatterers. As a result, errors in the minimization routine due to errors in the attenuation-compensation function are less significant when estimating the size of the glass beads. This would result in a decrease in the improvement provided by the new generalized attenuation-compensation function.

In order to test whether the use of glass beads instead of scatterers with Gaussian impedance distributions was responsible for the loss in improvement between our earlier simulation study[7] and the current experimental study, simulations were run using glass beads for the scatterers. However, the sources were still assumed to be diffraction limited whose velocity potential fields had a three-dimensional Gaussian distribution at the focus. Hence, w_z was given by $6.01\lambda f\#^2$, and $w_{x,y}$ was given by $w_x = w_y = 0.87\lambda f\#$. In the new simulations, the attenuation, sound speed, and scatterer concentration were set to the values determined for the phantom. Likewise, the radius of the shells was set at 24.5 μm. One thousand independent scatterer distributions were generated yielding 1000 independent backscattered waveforms. The waveforms were then separated into 40 independent sets with 25 waveforms per set. Each set was then processed to yield 40 independent estimates for the scatterer size.

The simulated sources were also excited by an impulse spike (to model the Panametrics pulse) and had Rayleigh frequency responses found by fitting a Rayleigh distribution [i.e., $f \cdot \exp(-((f-f_R)/\sigma_R)^2)$] to the measured frequency spectrum from the reflection off of the rigid plane at the focus. This was done so that the resulting spectrum of the simulated sources would be as close as possible to the real sources. The bandwidth used in the estimate, however, consisted of the frequencies in the range between 6.5 and 10.5 MHz as was done for the experimental results. Other source parameters, including the depth at which the focus was placed in the simulated phantom, were identical to those provided in Table I.

A plot showing the simulated phantom results is given in Fig. 5. The differences between the different attenuation-compensation functions are greatly reduced. For the $f/4$ transducer at a window length of 13 mm, the difference between the size estimate given by A_{OM} and A_{comp} is 6.4% compared to 7.1% for the experimental results. Likewise, A_{OO} and A_{PC} gave simulated differences from A_{comp} of 2.9% and -1.75%, respectively, comparable to the experimental differences of 1.8% and -5.6%. Similarly, the $f/2$ transducer at a window length of 13 mm gave simulated differences from A_{comp} of 18% for A_{OM}, 15.6% for A_{OO}, and 12.4% for A_{PC} that were very close to the differences of 18.4%, 15.5%, and 11.5%, respectively, that were found experimentally. Therefore, the decrease in improvement discussed previously (i.e., % difference of 12% to 18% instead of 40% to 50% for the $f/2$) can be directly attributed to the type of scatterer being measured. This is of great importance for estimating scatterer sizes of biological tissue because the fundamental scatterer geometry (type) in tissue has not been determined. Hence, the improvement of the new generalized attenuation-compensation function compared to the traditional attenuation-compensation functions may be even more significant in a clinical setting because the correct scatterer geometry may exhibit an even stronger dependence on the attenuation-compensation function.

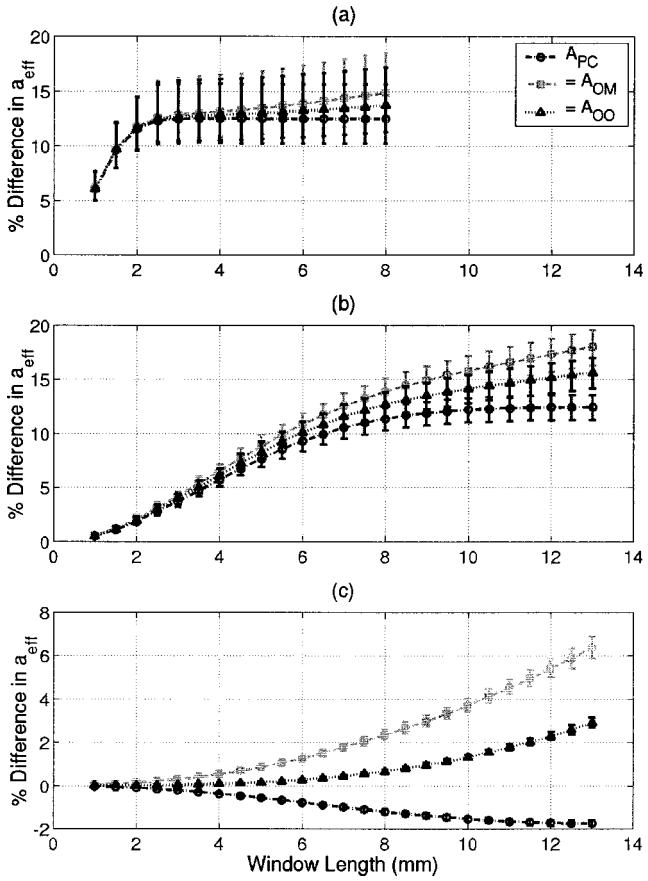

FIG. 5. Simulation results for % difference in a_{eff} found using traditional attenuation-compensation functions (A_{PC}, A_{OM}, and A_{OO}) as compared to a_{eff} found using A_{comp} for a glass bead phantom with an attenuation of 0.55 ± 0.08 dB/cm/MHz, a concentration of 20.454 beads/mm^3, and bead radius of 24.5 μm from spherically focused transducers with *f*-numbers of (a) $f/1$, (b) $f/2$, and (c) $f/4$, and $w_z = 6.01\lambda f\#^2$.

C. Effect of wavelength dependence of focusing

Although the type of scatterer and the subsequent dependence on the attenuation-compensation function explains the reduction in the improvement provided by the new attenuation compensation function, it does not explain why the plateau of the $f/1$ transducer (i.e., difference from A_{comp} for A_{PC} of 3.4%) was different than the plateau for the $f/2$ transducer (i.e., difference from A_{comp} for A_{PC} of 11.5%). The previous simulation study (Sec. III B) showed them converging to the same value whereas, in the experiment, they converged to different amounts of improvement. In order to understand this behavior, we explore another difference between the previous simulation studies and the experimen-

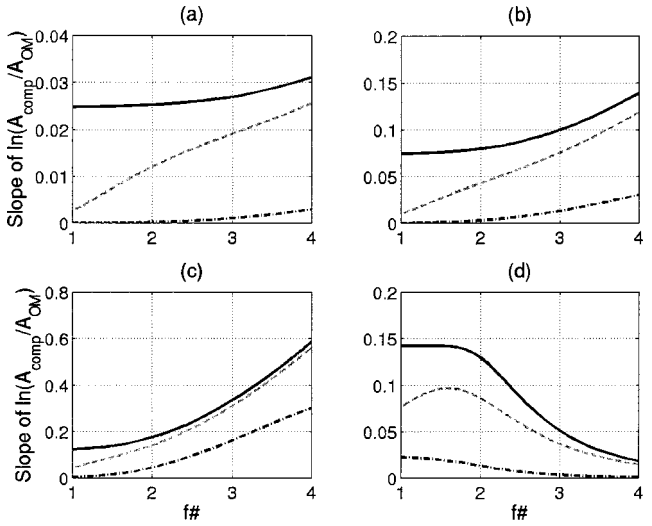

FIG. 6. Calculated slope of $\ln(A_{comp}/A_{OM})$ versus frequency for transducers with varying degrees of focusing (i.e., $f\#$). The three curves in the plots correspond to w_z values with three different dependencies on wavelength; ——— for $w_z = 6.01(f\#)^2 \cdot \lambda$, – – – for $w_z = 6.01(f\#)^2 \cdot \lambda + 1285\ \mu$m, and -·- for $w_z = 6.01(f\#)^2 \cdot (181\ \mu\text{m})$. The plots had (a) window length normalized to the depth of focus (i.e., $7.08\lambda_0 f\#^2$) of 0.5, (b) window length normalized to the depth of focus (i.e., $7.08\lambda_0 f\#^2$) of 1, (c) window length normalized to the depth of focus (i.e., $7.08\lambda_0 f\#^2$) of 2.5, and (d) window length of 8 mm.

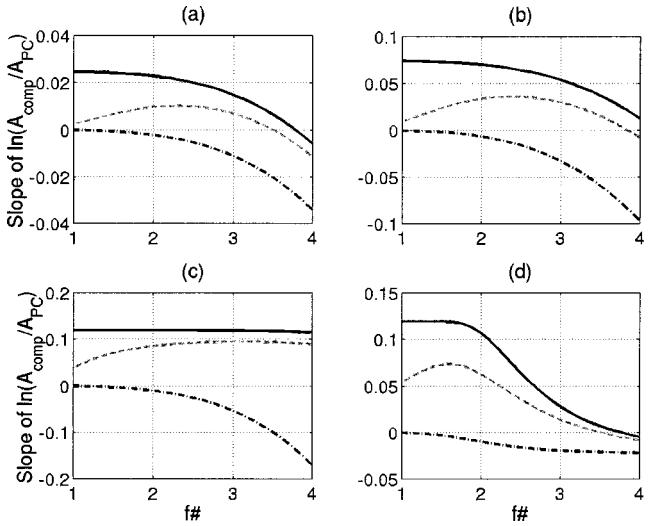

FIG. 7. Calculated slope of $\ln(A_{comp}/A_{PC})$ versus frequency for transducers with varying degrees of focusing (i.e., $f\#$). The three curves in the plots correspond to w_z values with three different dependencies on wavelength; ——— for $w_z = 6.01(f\#)^2 \cdot \lambda$, – – – for $w_z = 6.01(f\#)^2 \cdot \lambda + 1285\ \mu$m, and -·- for $w_z = 6.01(f\#)^2 \cdot (181\ \mu\text{m})$. The plots had (a) window length normalized to the depth of focus (i.e., $7.08\lambda_0 f\#^2$) of 0.5, (b) window length normalized to the depth of focus (i.e., $7.08\lambda_0 f\#^2$) of 1, (c) window length normalized to the depth of focus (i.e., $7.08\lambda_0 f\#^2$) of 2.5, and (d) window length of 8 mm.

tal study: the wavelength dependence of the effective Gaussian depth of focus along the beam, axis, w_z. In the earlier simulations, w_z was directly proportional to the wavelength [i.e., $w_z = 6.01(f\#)^2 \cdot \lambda$], but, in the experiment, w_z had the form

$$w_z = w_{zm} \cdot \lambda + w_{zb}, \tag{5}$$

where w_{zb} was a constant independent of wavelength (Table I).

In order to understand the impact of the wavelength dependence of w_z, the curves of $\ln(A_{comp}/A_{OM})$ and $\ln(A_{comp}/A_{PC})$ versus frequency were fit by a line. The slope of this line could then be used to predict how the scatterer size estimate from A_{comp} would compare to the estimate from A_{OM} and A_{PC}. A positive slope means that the estimate from $A_{PC/OM}$ is larger than the estimate obtained from A_{comp}. Likewise, a negative slope means that the estimate from $A_{PC/OM}$ is smaller than the estimate from A_{comp}. The wavelength dependence of w_z was evaluated for three different w_z values: (a) $6.01(f\#)^2 \cdot \lambda$, as was used in the previous simulation study,[7] (b) $6.01(f\#)^2 \cdot \lambda + 1285\ \mu$m, similar to the wavelength dependence found for the measured transducers, and (c) $6.01(f\#)^2 \cdot (181\ \mu\text{m})$. The calculations were performed for window lengths normalized to the traditional depth of focus (i.e., $7.08\lambda_0 f\#^2$) of 0.5, 1, and 2.5 as well as for a window length of 8 mm. The resulting slopes are shown in Figs. 6 and 7.

Consider first the w_z values of $6.01(f\#)^2 \cdot \lambda$ shown by the solid curves. For any given normalized window length, the A_{OM} estimate is larger than the A_{comp} estimate and increases with increasing *f*-number. Likewise, the A_{PC} estimate is larger than the A_{comp} estimate for smaller *f*-numbers and then decreases with increasing *f*-number for smaller normalized window lengths resulting in the A_{PC} estimate being smaller than the A_{comp} estimate. For larger normalized window lengths, the A_{PC} estimate is always larger than the A_{comp} estimate and there is no longer any dependency on *f*-number corresponding to the plateau observed earlier.

Now consider the w_z values illustrated by the remaining curves. The sizes of the $A_{PC/OM}$ estimates relative to the size of the A_{comp} estimate are reduced as the wavelength dependency of w_z is reduced as is illustrated by the dash-dot-dash curve $[6.01(f\#)^2 \cdot \lambda + 1285\ \mu\text{m}]$ being lower than the dashed curve $[6.01(f\#)^2 \cdot (181\ \mu\text{m})]$. Also, for w_z given by $6.01(f\#)^2 \cdot \lambda + 1285\ \mu$m, the estimates approach the $6.01(f\#)^2 \cdot \lambda$ curve for larger *f*-number and approach the $6.01(f\#)^2 \cdot (181\ \mu\text{m})$ curve for smaller *f*-number. As a result, the A_{PC} estimates no longer plateau independent of *f*-number. Therefore, the $f/1$ transducer used in the experiment should have yielded a smaller difference between the A_{PC} and A_{comp} estimates than the $f/2$ transducer, just as was observed, due to its weaker dependence on wavelength.

The results for A_{PC} as compared to A_{comp} at large normalized window lengths can also be shown mathematically. For sufficiently large window lengths, the integral along the beam axis in A_{comp} can be evaluated in closed form, yielding

$$A_{comp}(\omega) = \frac{2}{w_z\sqrt{\pi}} e^{4\alpha_{\text{eff}} z_T} e^{-\alpha^2 w_z^2}. \tag{6}$$

Hence, the derivative of $\ln(A_{comp}/A_{PC})$ versus frequency is given by

$$\frac{\partial}{\partial f}\left\{\ln\left(\frac{A_{comp}}{A_{PC}}\right)\right\} = -\frac{1}{w_z}\frac{\partial w_z}{\partial f} - 2(\alpha w_z) \times\left[w_z\frac{\partial \alpha}{\partial f} + \alpha\frac{\partial w_z}{\partial f}\right], \tag{7}$$

which can be simplified to

$$\frac{\partial}{\partial f}\left\{\ln\left(\frac{A_{comp}}{A_{PC}}\right)\right\} = \frac{w_{zm}c(f^{-2})}{w_{zm}\cdot\lambda + w_{zb}} + \left[2\alpha^2[w_{zm}\cdot\lambda + w_{zb}]w_{zm}c(f^{-2}) - 2\alpha[w_{zm}\cdot\lambda + w_{zb}]^2\frac{\partial\alpha}{\partial f}\right] \tag{8}$$

if w_z has the form given in Eq. (5). Hence, the significance of the wavelength dependence of w_z is also affected by the magnitude and frequency dependence of the attenuation. For the purpose of comparison, we will assume that the attenuation has a strict linear frequency dependence (i.e., $\alpha = \alpha_o \cdot f$), allowing Eq. (8) to be rewritten as

$$\frac{\partial}{\partial f}\left\{\ln\left(\frac{A_{comp}}{A_{PC}}\right)\right\} = \frac{1}{f}\left(\frac{w_{zm}\cdot\lambda}{w_{zm}\cdot\lambda + w_{zb}}\right) - 2\alpha_o^2 f w_{zb}[w_{zm}\cdot\lambda + w_{zb}]. \tag{9}$$

Hence, if $w_{zb}=0$, then the slope of $\ln(A_{comp}/A_{PC})$ versus frequency is equal to $1/f$ and is independent of the value of w_{zm}. Likewise, if $w_{zm}=0$, then the slope of $\ln(A_{comp}/A_{PC})$ versus frequency decreases approximately parabolically with increasing values of w_{zb}. Both of these effects are evident in Fig. 7(c).

In order to further test the impact of the wavelength dependence of w_z on the different attenuation-compensation functions, the simulation of the glass bead phantoms was repeated using the w_z values found experimentally. Once again, the attenuation, sound speed, and scatterer concentration were set to the values determined for the phantom, and the radius of the shells was set at 24.5 μm. Also, 40 independent estimates were obtained for 1000 independent scatterer distributions that were generated and then processed in groups of 25 using frequencies in the range between 6.5 and 10.5 MHz. The simulated sources were also modeled to have the same Rayleigh frequency response as was found experimentally and were excited by an impulse spike. The resulting differences between the different attenuation-compensation functions are shown in Fig. 8.

Once the measured values for w_z were used in the simulations, the differences between A_{comp} and the other attenuation-compensation functions for the $f/1$ transducer at 8 mm were 7.4%, 5.9%, and 4.3% whereas the differences for the $f/2$ transducer at 13 mm were 16%, 13.4%, and 10% for A_{OM}, A_{OO}, and A_{PC}, respectively. Hence, A_{PC} for the $f/1$ transducer and the $f/2$ transducer now plateau at different levels in agreement with the observed experimental results. Therefore, the wavelength dependence of w_z was responsible for their earlier discrepancy. Furthermore, the differences found experimentally and the mean differences found in the simulations using the correct value for w_z were consistently within 2.5% of each other, validating the theoretical analysis provided in the companion paper.[7]

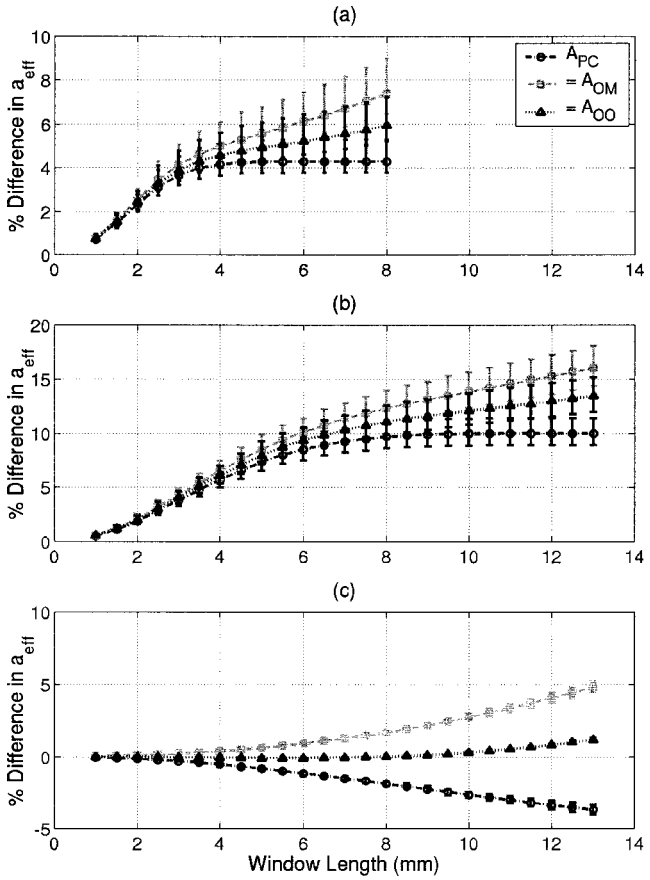

FIG. 8. Simulation results for % difference in a_{eff} found using the traditional attenuation-compensation functions (A_{PC}, A_{OM}, and A_{OO}) as compared to a_{eff} found using A_{comp} for a glass bead phantom with an attenuation of 0.55 ± 0.08 dB/cm/MHz, a concentration of 20.454 beads/mm^3, and bead radius of 24.5 μm from spherically focused transducers with *f*-numbers of (a) $f/1$, (b) $f/2$, and (c) $f/4$, and w_z as given in Table I.

IV. CONCLUSIONS

In this paper, we further explored the use of focused sources for estimating scatterer sizes. First, we compared two different methods to calibrate a focused source, and found that simply recording/processing the echoes from a rigid plane moved along the beam axis could yield sufficient calibration information. This calibration routine is a straightforward extension to the current calibration techniques used to obtain a reference in scatterer size estimates.[2,3,5,10] Then, we attempted to validate our previous theoretical work by using real focused transducers to estimate the size of glass beads in a tissue mimicking phantom. We found agreement better than 2.5% provided that the same type of scatterers and sources were being compared. Errors in the attenuation-compensation function when estimating the radius of the glass beads were much less significant than the same errors when estimating the radius of a Gaussian scatterer, indicating a strong dependence on the type of scatterer when assessing the accuracy of any attenuation-compensation function. Lastly, we explored the effects of focusing in greater detail

and found that the improvement provided by the new generalized attenuation-compensation function decreases as the wavelength dependence of w_z was reduced.

The dependence of the performance of the attenuation-compensation function on the scatterer type is very important in light of the reference phantom technique that has recently been proposed to correct for focusing when estimating the characteristic size of the tissue microstructure.[12] Namely, tissue mimicking phantoms with glass beads should not be used to test the validity of the reference phantom technique as an attenuation-compensation method because the estimation of glass bead radius has a very weak dependence on the attenuation-compensation function. Hence, if the reference phantom technique introduces large errors into the compensation for attenuation and focusing, these errors will not be detected in phantom experiments using glass beads. Ideally, the assessment should be done using real tissue. However, the real size of scatterers in tissue is not known, so simulation studies similar to those presented in this paper may have to suffice. Another possibility would be to use tissue while using our generalized attenuation-compensation function as a standard to which the reference phantom results could be compared.

From these results, it is clear that weakly focused sources are not required when estimating the scatterer size even for window lengths much greater than the depth of focus for the source. Because increased focusing provides for increased signal-to-noise ratios and better lateral resolution, focused sources may perform better when quantifying the size of the tissue microstructure. However, the exact effect of focusing on signal-to-noise ratios as it applies to scatterer size estimation remains to be quantified.

ACKNOWLEDGMENTS

A special thanks to Deepti Narla for her help in acquiring the wire reflection data. This work was supported by the University of Illinois Research Board, by a NDSEG Fellowship awarded to T. A. Bigelow, and by a Beckman Institute Graduate Fellowship awarded to T. A. Bigelow.

[1] T. Wang, J. Saniie, and X. Jin, ''Analysis of low-order autoregressive models for ultrasonic grain signal characterization,'' IEEE Trans. Ultrason. Ferroelectr. Freq. Control **38**(2), 116–124 (1991).
[2] M. L. Oelze, J. F. Zachary, and W. D. O'Brien, Jr., ''Characterization of tissue microstructure using ultrasonic backscatter: theory and technique optimization using a Gaussian form factor,'' J. Acoust. Soc. Am. **112**, 1202–1211 (2002).
[3] F. L. Lizzi, M. Greenebaum, E. J. Feleppa, and M. Elbaum, ''Theoretical framework for spectrum analysis in ultrasonic tissue characterization,'' J. Acoust. Soc. Am. **73**, 1366–1373 (1983).
[4] M. F. Insana and T. J. Hall, ''Parametric ultrasound imaging from backscatter coefficient measurements: image formation and interpretation,'' Ultrason. Imaging **12**, 245–267 (1990).
[5] M. F. Insana, R. F. Wagner, D. G. Brown, and T. J. Hall, ''Describing small-scale structure in random media using pulse-echo ultrasound,'' J. Acoust. Soc. Am. **87**, 179–192 (1990).
[6] F. L. Lizzi, M. Astor, T. Liu, C. Deng, D. J. Coleman, and R. H. Silverman, ''Ultrasonic spectrum analysis for tissue assays and therapy evaluation,'' Int. J. Imaging Syst. Technol. **8**, 3–10 (1997).
[7] T. A. Bigelow and W. D. O'Brien, Jr., ''Scatterer size estimation in pulse-echo ultrasound using focused sources: Theoretical approximations and simulation analysis,'' J. Acoust. Soc. Am. **116**, 578–593 (2004).
[8] P. Chaturvedi and M. F. Insana, ''Error bounds on ultrasonic scatterer size estimates,'' J. Acoust. Soc. Am. **100**, 392–399 (1996).
[9] K. Raum and W. D. O'Brien, Jr., ''Pulse-echo field distribution measurement technique for high-frequency ultrasound sources,'' IEEE Trans. Ultrason. Ferroelectr. Freq. Control **44**(4), 810–815 (1997).
[10] E. L. Madsen, M. F. Insana, and J. A. Zagzebski, ''Method of data reduction for accurate determination of acoustic backscatter coefficients,'' J. Acoust. Soc. Am. **76**, 913–923 (1984).
[11] E. L. Madsen, F. Dong, G. R. Frank, B. S. Garra, K. A. Wear, T. Wilson, J. A. Zagzebski, H. L. Miller, K. Kirk Shung, S. H. Wang, E. J. Feleppa, T. Liu, W. D. O'Brien, Jr., K. A. Topp, N. T. Sanghvi, A. V. Zaitsev, T. J. Hall, J. B. Fowlkes, O. D. Kripfgans, J. G. Miller, ''Interlaboratory comparison of ultrasonic backscatter, attenuation, and speed measurements,'' J. Ultrasound Med. **18**, 615–631 (1999).
[12] A. Gerig, J. Zagzebski, and T. Varghese, ''Statistics of ultrasonic scatterer size estimation with a reference phantom,'' J. Acoust. Soc. Am. **113**, 3430–3437 (2003).